

Supplementary Information for
Superthermal Solar Interfacial Evaporation is not due to Reduced Latent
Heat of Water

James H. Zhang^a, Rohith Mittapally^a, Guangxin Lv,^a Gang Chen^{a*}

^aMechanical Engineering Department, Massachusetts Institute of Technology,
Cambridge, MA 02139

*Corresponding author: gchen2@mit.edu

This file includes:

Supplementary Note S.1-S.7

Figures S1 to S13

Tables S1 to S2

References 1 to 17

Supplementary Note S.1

Estimation of temperature difference to cause convective mixing in water

Due to the cold evaporating top surface and relatively warmer temperature of water on the bottom, the unstable density stratification in the liquid water causes natural convection currents to form. Laminar flow of water inside the container will cause mixing and lead to a more isothermal temperature distribution.

The water in the container can be treated as in an enclosure heated on the bottom and sidewalls and cooled on the top surface from evaporation. A critical Rayleigh number commonly cited for convection to take place for a free top surface and rigid bottom surface is¹

$$Ra_H \geq 1100 \quad (S1.1)$$

Using the thermophysical properties of water, we can solve for the ΔT that will lead to convection.

$$\Delta T = \frac{1100\alpha\nu}{g\beta H^3} = 0.0012 \text{ K} \quad (S1.2)$$

where g is gravity, β is the thermal expansion of water, H is the height between the hot bottom and cold top, α is the thermal diffusivity of water, and ν is the kinematic viscosity of water. Plugging in values, we can find the critical ΔT is 1.2 mK.

Supplementary Note S.2

Correlation Model to Predict Water-Only Natural Evaporation

We will construct a simplified model to estimate the evaporation rates from a pure water surface. The full heat and mass transfer diagram is illustrated in Fig. S2. To model the top air side heat transfer, we will use Kadambi and Drake's correlation for circular cold plate in hot environment.^{2,3} We will assume that the heat and mass transfer analogies hold, so that the same correlation can model both the Sherwood number and the Nusselt number.

$$Sh_D = 0.82Gr_D^{0.2}Sc^{0.234} \quad (S2.1)$$

$$Nu_D = 0.82Gr_D^{0.2}Pr^{0.234} \quad (S2.2)$$

D is the diameter of the evaporating surface, Gr is the Grashof number, Sc is the Schmidt number, and Pr is the Prandtl number. Since squares and circles have the same area to perimeter ratio, the same values can be calculated for squares but instead using its side-length. The Sherwood and Nusselt numbers can be related to the air side heat and mass transfer coefficients through

$$g_m = \frac{Sh_D D_v}{D} \quad (S2.3)$$

$$h_{air} = \frac{Nu_D k_{air}}{D} \quad (S2.4)$$

where D_v is the diffusion coefficient of water vapor in excess of air and k_{air} is the thermal conductivity of air. The heat and mass transfer coefficients can be used to find the air side heat transfer and evaporation rate through Eqs. (S2.5-S2.7).

$$\dot{m} = g_m A_c C_g \left(c_{v,s}(T_s) - (RH)c_{v,s}(T_\infty) \right) \quad (S2.5)$$

$$q_{evap} = \dot{m} h_{fg}(T_s) \quad (S2.6)$$

$$q_{air} = h_{air} A_c (T_\infty - T_s) \quad (S2.7)$$

where A_c is the cross-sectional area, C_g is the molar density of dry air, $c_{v,s}$ is the saturated vapor mole fraction at a certain temperature, RH is the ambient relative humidity, h_{fg} is the latent heat of evaporation, T_s is the evaporating surface temperature, and T_∞ is the ambient temperature. Radiation exchange between the top surface and the ambient is modeled using the typical heat transfer between a surface and a large gray body reservoir.

$$q_{rad} = h_{rad} A_c (T_\infty - T_s) \quad (S2.8)$$

where h_{rad} is

$$h_{rad} = \sigma \epsilon_w (T_\infty^2 + T_s^2)(T_\infty + T_s) \quad (S2.9)$$

σ is the Stefan-Boltzmann constant and ϵ_w is the blackbody emissivity of water. Heat transfer through the water pathway is modeled as a resistance network from the outside ambient air to the evaporating top surface. This leads to the general heat transfer equation to become

$$q_{water} = \frac{(T_{\infty} - T_s)}{R_{water}} \quad (S2.10)$$

where R_{water} is the total resistance of the bottom pathway from the ambient environment to the evaporating surface. We assume that the bulk water is isothermal with its surface temperature due to convective flows, leading to temperature differences only occurring at the boundary layers near the container walls. The heat transfer resistance from the ambient environment through the water to the surface comes from two parallel pathways: the bottom of the container and the side of the container.

$$\frac{1}{R_{water}} = \frac{1}{R_{bot}} + \frac{1}{R_{side}} \quad (S2.11)$$

The convective flow boundary layers of water on the sidewalls and the bottom container wall should be coupled due to the Rayleigh-Bernard convection cell, however, we will calculate the heat transfer through each boundary layer separately due to the lack of heat transfer empirical correlations for the prescribed flow conditions. The resistance through the bottom is a series resistance of the aluminum scale pan (Supplementary Note S.7), acrylic container wall, and natural convection from the warmer acrylic container bottom into the colder water.

$$R_{bot} = R_p + \frac{1}{A_c} \left(\frac{t_{cont}}{k_{acry}} + \frac{1}{h_{bot}} \right) \quad (S2.12)$$

where R_p is the effective heat transfer resistance from the aluminum scale pan found in SI Note 7. The convective heat transfer coefficient from the bottom of the acrylic container to the water was approximated using Raithby and Hollands' correlation for a hot plate in cold fluid environment.^{3,4}

$$h_{bot} = \frac{Nu_{L^*,corr} k_{water}}{L^*} \quad (S2.13)$$

$$Nu_{L^*,bot} = \frac{0.56 Ra_{L^*,water}^{1/4}}{(1 + (0.492/Pr_{water})^{9/16})^{4/9}} \quad (S2.14)$$

Due to the low Nusselt numbers expected from the small temperature differences, the Nusselt number in Eq. (S2.14) is corrected using the following equation.³

$$Nu_{L^*,corr} = \frac{1.4}{\ln \left(1 + \frac{1.4}{Nu_{L^*,bot}} \right)} \quad (S2.15)$$

The characteristic number used for Raithby and Hollands correlation is based on the area to perimeter ratio of the bottom surface.^{3,5}

$$L^* = \frac{A_c}{P} = \frac{D}{4} \quad (S2.16)$$

The heat transfer through the sidewalls has three heat transfer resistances in series: air side convection, acrylic sidewall, and water convection.

$$R_{side} = \frac{1}{A_p} \left(\frac{t_{acry}}{k_{acry}} + \frac{1}{h_{side,air}} + \frac{1}{h_{side,water}} \right) \quad (S2.17)$$

Both the air and water natural convection correlations on the sidewalls were evaluated using Churchill and Chu's correlation for a vertical wall in natural convective conditions for the respective fluid thermophysical properties.⁶

$$Nu_{H,side} = 0.68 + \frac{0.67Ra_H^{1/4}}{(1 + (0.492/Pr)^{9/16})^{4/9}} \quad (S2.18)$$

$$h_{side,air} = \frac{Nu_{H,side}k_{air}}{H} \quad (S2.19)$$

$$h_{side,water} = \frac{Nu_{H,side}k_{water}}{H} \quad (S2.20)$$

where Ra is the Rayleigh number describing the natural convective flow. For these calculations, we made the thin wall approximation to neglect the changing thickness due to the curvature of the container.

$$t_{acry} \ll D \quad (S2.21)$$

All fluid properties, non-dimensional numbers, convective heat transfer coefficients, and convective mass transfer coefficients are evaluated at the mean temperature between the wall temperature and the bulk fluid temperature it is in contact with.

$$T_{film} = \frac{(T_{fluid} + T_{wall})}{2} \quad (S2.22)$$

As a result, the temperature of the evaporating surface, T_s , can be found through energy balance on the surface temperature node.

$$0 = -q_{evap} + q_{air} + q_{rad} + q_{water} \quad (S2.23)$$

This equation can be used to solve for the unknown surface temperature for a given geometry and two boundary conditions of the ambient RH and ambient temperature using nonlinear zero solvers. The evaporation rate can then be found by using Eq. (S2.5) for the calculated surface temperature.

Supplementary Note S.3

Correlation Model to Predict Porous Sample Evaporation

The addition of a porous material will have two effects on the overall heat transfer in the model: additional heat transfer resistances through the bottom waterside pathway and the inclusion of intermediate water states. The full heat and mass transfer diagram is shown in Fig S5 with all temperature and vapor concentration node labels. At the top interface, Eq. (S2.23) and q_{water} from Eq. (S2.10) must be modified to account for the thermal insulation effect and reduced latent heat effects.

First, if there are no reduced latent heat effects as seen for the base case porous sample evaporation, two additional heat transfer resistances that are in series with the original heat transfer resistance through the water need to be added, leading to q_{water} in Eq. (S2.10) being replaced with q_{samp} .

$$q_{samp} = \frac{(T_{\infty} - T_s)}{R_{water} + R_{s,w} + \frac{t_{samp}}{k_{samp}A_c}} \quad (S3.1)$$

The addition of the porous materials will create another boundary layer at the surface where water and the sample are in contact, leading to the additional thermal resistance $R_{s,w}$.

$$R_{s,w} = \frac{1}{h_{s,w}A_c} \quad (S3.2)$$

At the sample-water interface with temperature $T_{s,w}$, the water density stratification is not stable due to the bulk water, T_w , having a warmer temperature. As a result, $h_{s,w}$ can be described using Raithby and Hollands' correlation with the corresponding film properties in Eq. (S2.14-2.16). We will ignore the detailed flow of water inside of the porous evaporator and lump it into the sample's effective thermal conductivity, leading to the third thermal resistance term in Eq. (S3.1). This is because the average net liquid water flow velocity is very small due to the low evaporation rates expected from natural evaporation. Since the evaporating surface is no longer a water-only interface, the surface temperature T_s is not equal to the bulk water temperature T_w . All other equations for describing R_{water} , q_{rad} , q_{evap} , and q_{air} in Supplementary Note S.2 still hold.

Eq. (S3.1) is only true if there is no cooling effect at the sample-water interface due to the enthalpy difference between bulk water and intermediate water states from reduced latent heat. If reduced latent heat effects are to be included, energy balance needs to be applied at the surface temperature node T_s and the sample-water interface temperature node $T_{s,w}$. At the surface temperature node, Eq. (S2.23) becomes

$$0 = -\chi q_{evap} + q_{air} + q_{rad} + \frac{k_{samp}A_c}{t_{samp}}(T_{s,w} - T_s) \quad (S3.3)$$

and at the sample-water interface

$$0 = -\frac{k_{samp}A_c}{t_{samp}}(T_{s,w} - T_s) + \frac{(T_{\infty} - T_{s,w})}{R_{s,w} + R_{water}} - (1 - \chi)q_{evap} \quad (S3.4)$$

To account for the reduced latent heat of evaporation of intermediate water χ , a cooling effect occurs at the sample and water interface due to the enthalpy difference between bulk water and intermediate water. For simplicity of this analysis, we set the enthalpy of the intermediate state to be halfway between bulk liquid and water, leading to a latent heat of evaporation reduction of 50% ($\chi=0.5$). As a result, we distribute the evaporation heat flux, q_{evap} , equally to the top and bottom side of the sample. We then solve these equations to find the evaporation rate of porous evaporators. This analysis assumes that the surface of the interfacial evaporator is fully wetted and hydrodynamically smooth. Hydrodynamically smooth refers to the surface roughness characteristic size to be small when compared to the momentum boundary layers.

Supplementary Note S.4

Correlation Model to Predict Porous Sample Solar Evaporation without Reduced Latent Heat

In solar evaporation, the top side of the porous evaporator is now a hot surface in a cold environment. As a result, we will now use Raithby and Holland's correlation to estimate the top air side heat transfer evaporation using the heat and mass transfer analogy again.^{3,4}

$$Nu_{L^*,air} = \frac{0.56Ra_{L^*}^{1/4}}{(1 + (0.492/Pr)^{9/16})^{4/9}} \quad (S4.1)$$

$$Sh_{L^*,evap} = \frac{0.56Gr_{L^*}^{1/4}Sc^{1/4}}{(1 + (0.492/Sc)^{9/16})^{4/9}} \quad (S4.2)$$

Due to the low Rayleigh numbers expected, the $Nu_{L^*,air}$ is corrected again using Eq. (S2.15). $Sh_{L^*,air}$ will be corrected using the same equation.

$$Sh_{L^*,corr} = \frac{1.4}{\ln\left(1 + \frac{1.4}{Sh_{L^*,evap}}\right)} \quad (S4.3)$$

Thus, the heat and mass transfer on the top side of the porous evaporator, q_{air} , \dot{m}_{evap} , and q_{evap} can be described by using the corrected Nusselt numbers and Sherwood numbers in Eqs. (S4.1-4.3).

Since there is no convection in water due to the stable density stratification, we can treat heat transfer in water as due to conduction only. In this case, the Biot number in the radial direction, $Bi = h_{eff}R/k_w$, is ~ 0.25 . Hence, we can approximate water as a fin with temperature variation only along the height z-direction, described by the fin equation

$$\frac{d^2T_w}{dz^2} = \frac{h_{eff}P}{k_wA_c}(T_w - T_\infty) \quad (S4.4)$$

where we define the base of the fin as the interface between the sample and water and the z-axis to point downwards. The effective heat transfer coefficient, h_{eff} , includes the resistance of the container wall as well as the natural convection coefficient.

$$h_{eff} = \frac{1}{\frac{t_{cont}}{k_{cont}} + \frac{1}{h_{side}}} \quad (S4.5)$$

Using a change of variables

$$\theta = T_w - T_\infty \quad (S4.6)$$

and integrating Eq. (S4.4) yields the general fin equation

$$\theta = c_1 e^{z \sqrt{\frac{h_{eff}P}{k_wA_c}}} + c_2 e^{-z \sqrt{\frac{h_{eff}P}{k_wA_c}}} \quad (S4.7)$$

The heat flux and temperature at the interfaces between the sample-water and sample-container bottom must be continuous, yielding four boundary conditions. At the sample-water interface

$$-k_{water} \frac{d\theta}{dz} \Big|_{z=0} = \frac{k_{samp}}{t_{samp}} (T_s - T_{s,w}) \quad (S4.8)$$

$$\theta(0) + T_\infty = T_{s,w} \quad (S4.9)$$

At the bottom-water interface

$$-A_c k_{water} \frac{d\theta}{dz} \Big|_{z=H} = q_{bot} \quad (S4.10)$$

$$\theta(H) + T_\infty = T_{bot} \quad (S4.11)$$

The heat transfer through the bottom of the container is

$$q_{bot} = \frac{(T_{bot} - T_\infty)}{R_p + \frac{t_{cont}}{k_{cont} A_c}} \quad (S4.12)$$

where T_{bot} is the temperature of the container bottom wall in contact with the water and R_p is the effective aluminum scale pan resistance found in SI Note 7. h_{side} in Eq. (S4.5) depends on the outer container wall temperature and there is a temperature distribution inside of the water, leading to the need to approximate h_{side} for this analysis. Using a 1D heat transfer network, we approximated the outer container wall temperature node T_o and h_{side} by doing an energy balance on the outer container wall temperature node. In this analysis, we assume that the inside wall temperature of the acrylic container is isothermal with the water: $T_i(z) = T_w(z)$.

$$T_{w,ave} = \frac{\int_0^H T_w(z) dz}{H} \quad (S4.13)$$

$$\frac{k_{cont}(T_{w,ave} - T_o)}{t_{cont}} = h_{side}(T_o - T_\infty) \quad (S4.14)$$

Eq. (S2.23) is modified to account for the solar absorption energy for energy balance at the sample-air interface.

$$0 = q_{sun} - q_{evap} + q_{air} + q_{rad} - \frac{k_{samp} A_c}{t_{samp}} (T_s - T_{s,w}) \quad (S4.15)$$

where q_{sun} is set to one-sun intensity.

$$q_{sun} = 1000 A_c \quad (S4.16)$$

q_{air} and q_{rad} have different signs because it is defined in Eq. (S2.7) and Eq. (S2.8) as the difference between the ambient temperature and the surface temperature. Since the surface temperature is hotter than ambient, these terms will become negative and sources of heat loss in Eq. (S4.15). The evaporation rate can then be solved by numerically solving for each of the temperature nodes and the unknown fin coefficients in Eq. (S4.7) by using the boundary conditions Eqs. (S4.8-4.11).

Supplementary Note S.5

Correlation Model to Predict Porous Sample Solar Evaporation with Reduced Latent Heat

Since the topside is hot, the heat transfer and mass transfer equations from Eqs. (S4.1-4.3) still hold for describing q_{air} and q_{evap} . However, the bottom interface of the porous evaporator will no longer be hot because of the mixing cooling effect when bulk water becomes an intermediate water state from reduced latent heat effects. As a result, the water temperature profile is no longer stratified in a stable density configuration and leads to natural convective mixing. This causes Eqs. (S4.4-4.10) to no longer hold. The energy balance on the top interface in Eq. (S4.14) becomes

$$0 = q_{sun} - \chi q_{evap} + q_{air} + q_{rad} - \frac{k_{samp} A_c}{t_{samp}} (T_s - T_{s,w}) \quad (S5.1)$$

where the latent heat of evaporation is reduced by half ($\chi=0.5$). At the bottom interface with temperature $T_{s,w}$, the energy balance becomes the same as Eq. (S3.4).

$$0 = \frac{k_{samp} A_c}{t_{samp}} (T_s - T_{s,w}) + \frac{(T_\infty - T_{s,w})}{R_{s,w} + R_{water}} - (1 - \chi) q_{evap} \quad (S5.2)$$

where T_w is the bulk water temperature. Eq. (S3.2) and Eqs. (S2.11-2.20) still hold to describe the heat transfer resistances from the boundary layer at the sample-water interface $R_{s,w}$ and the parallel heat transfer network from the ambient air into bulk water R_{water} .

Supplementary Note S.6

Correlation Model to Predict Porous Sample Solar Evaporation Under Forced Convection

For forced convection, Eqs. (S4.1-4.2) and (S2.18-2.19) will be modified to forced convection correlations. Since the airspeeds are likely to be low, we will be in the laminar regime. The heat and mass transfer above the evaporating surface will be approximated using crossflow over a flat plate correlation.³

$$Nu_{D,air} = 0.664Re_D^{1/2}Pr^{1/3} \quad (S6.1)$$

$$Sh_{D,evap} = 0.664Re_D^{1/2}Sc^{1/3} \quad (S6.2)$$

The sidewall heat transfer coefficient from air to the container wall will use the crossflow correlation for low Reynolds number flows against cylinders.^{7,8}

$$Nu_{D,side} = 0.3 + \frac{0.62Re_D^{1/2}Pr^{1/3}}{(1 + (0.42/Pr)^{2/3})^{1/4}} \quad (S6.3)$$

$$h_{side,air} = \frac{Nu_{D,side}k_{air}}{D} \quad (S6.4)$$

Supplementary Note S.7

Scale Pan Effective Thermal Resistance

Although in the FEA simulation, we assumed that the bottom surface is at ambient temperature, most experiments have the container bottom sitting on the surface of a weighing scale, and hence questions can be raised on how accurate is the assumption of constant ambient temperature at the bottom surface. In this case, ambient heat is transferred to the bottom via air convection onto the scale pan and conduction along the pan.

Due to the very laminar features, we will assume a constant natural convection coefficient of air of $1 \text{ W/m}^2\text{-K}$ on the aluminum pan for this analysis. Heat transfer through the bottom pathway goes through natural convection of the aluminum pan on the scale and into the water bottom. The scale's aluminum pan can be modeled as an annular fin.

$$k_p t_p \frac{\partial}{\partial r} \left(r \frac{\partial T}{\partial r} \right) - 2h(T - T_\infty) = 0 \quad (\text{S7.1})$$

The resulting equation then becomes

$$r \frac{\partial^2 T}{\partial r^2} + \frac{\partial T}{\partial r} - \frac{2hr}{k_p t_p} (T - T_\infty) = 0 \quad (\text{S7.2})$$

Using a change of variable

$$\theta = \frac{T - T_\infty}{T_b - T_\infty} \quad (\text{S7.3})$$

leads to

$$r \frac{\partial^2 \theta}{\partial r^2} + \frac{\partial \theta}{\partial r} - \frac{2hr}{k_p t_p} \theta = 0 \quad (\text{S7.4})$$

The boundary conditions for this equation are

$$\theta(r = r_c) = 1 \quad (\text{S7.4})$$

and

$$-k_p \frac{d\theta}{dr} \Big|_{r=r_p} = h\theta(r = r_p) \quad (\text{S7.5})$$

where r_c is the radius of the container and r_p is the radius of the aluminum pan. Assuming all the heat absorbed by the scale is transferred to the water container, the total heat from the annular aluminum plate fin to the base of the container is equal to

$$q_p^* = -k_p (2\pi r_c t_p) \frac{d\theta}{dr} \Big|_{r=r_c} \quad (\text{S7.6})$$

where r_c is the radius of the container t_p is the thickness of the aluminum pan. We can then recognize that this gives us an effective thermal resistance to describe heat transfer from the ambient air, through the aluminum pan, and into the bottom of the water container. First, we multiply both sides by $(T_b - T_\infty)$

and set q_p^* equal to the general heat transfer equation. This analysis assumes that the outer diameter of the pan reaches the ambient temperature.

$$q_p^*(T_b - T_\infty) = -k_p(2\pi r_c t_p) \frac{dT}{dr} = -\frac{(T_b - T_\infty)}{R_p} = q [W] \quad (S7.7)$$

where T_b is the temperature of the bottom of the container. By simple inspection, we can see that

$$R_p = -\frac{1}{q_p^*} \quad (S7.8)$$

By solving Eq. (S7.4) using the thermal conductivity of aluminum, a pan thickness of 1 mm, and a pan radius of 5 cm, we can estimate that

$$R_p = 68.898 \frac{K}{W} \quad (S7.9)$$

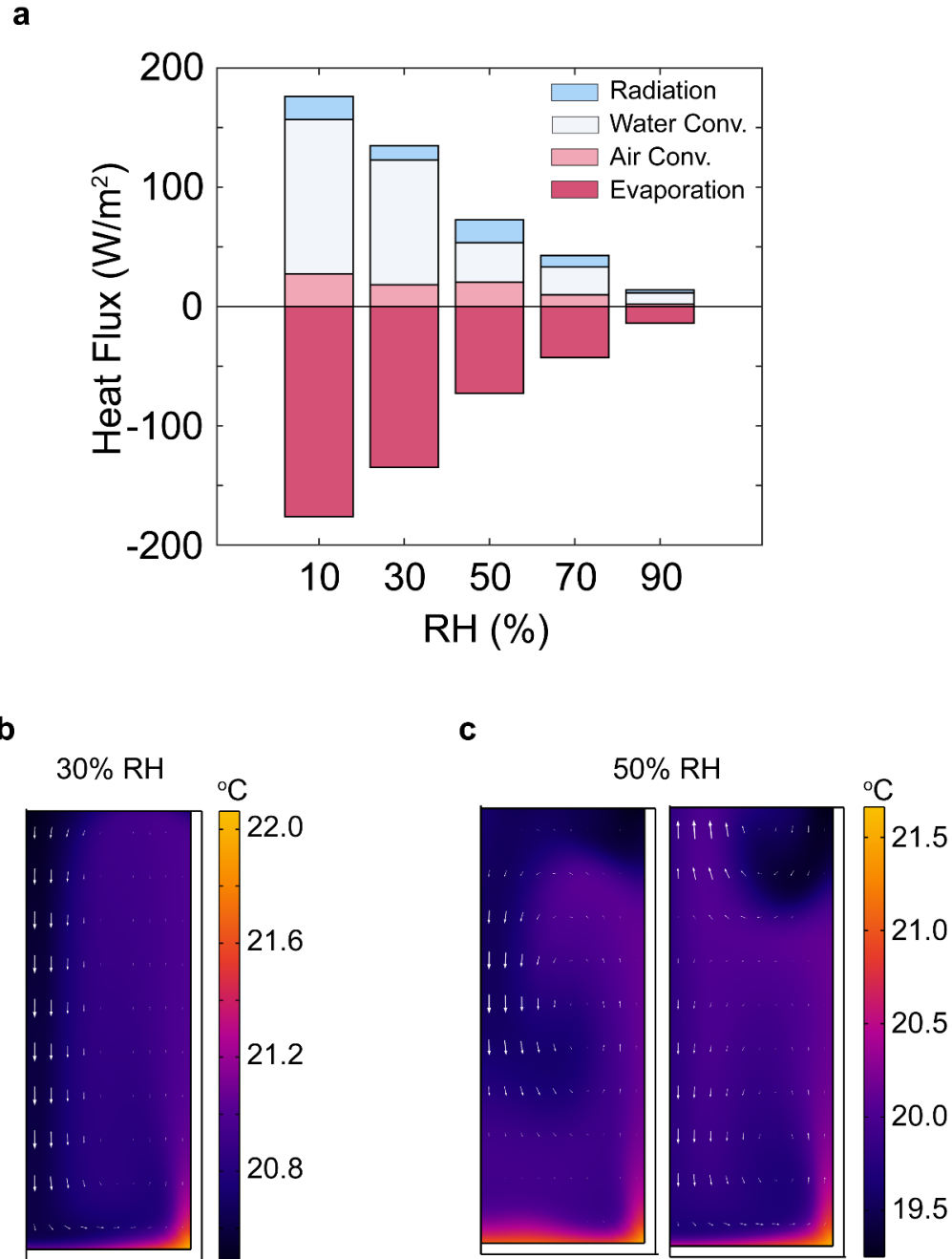


Fig. S1 Heat path for dark evaporation. (a) Heat fluxes from each of the pathways at the air-water interface in FEA simulations for a container with a diameter of 3 cm evaporating into an ambient at 23 °C. (b) Single cell natural convection pattern formed in liquid water container for 30% RH. (c) Oscillation between a weaker single cell (left) and two antisymmetric cells (right) natural convection patterns for 50% RH.

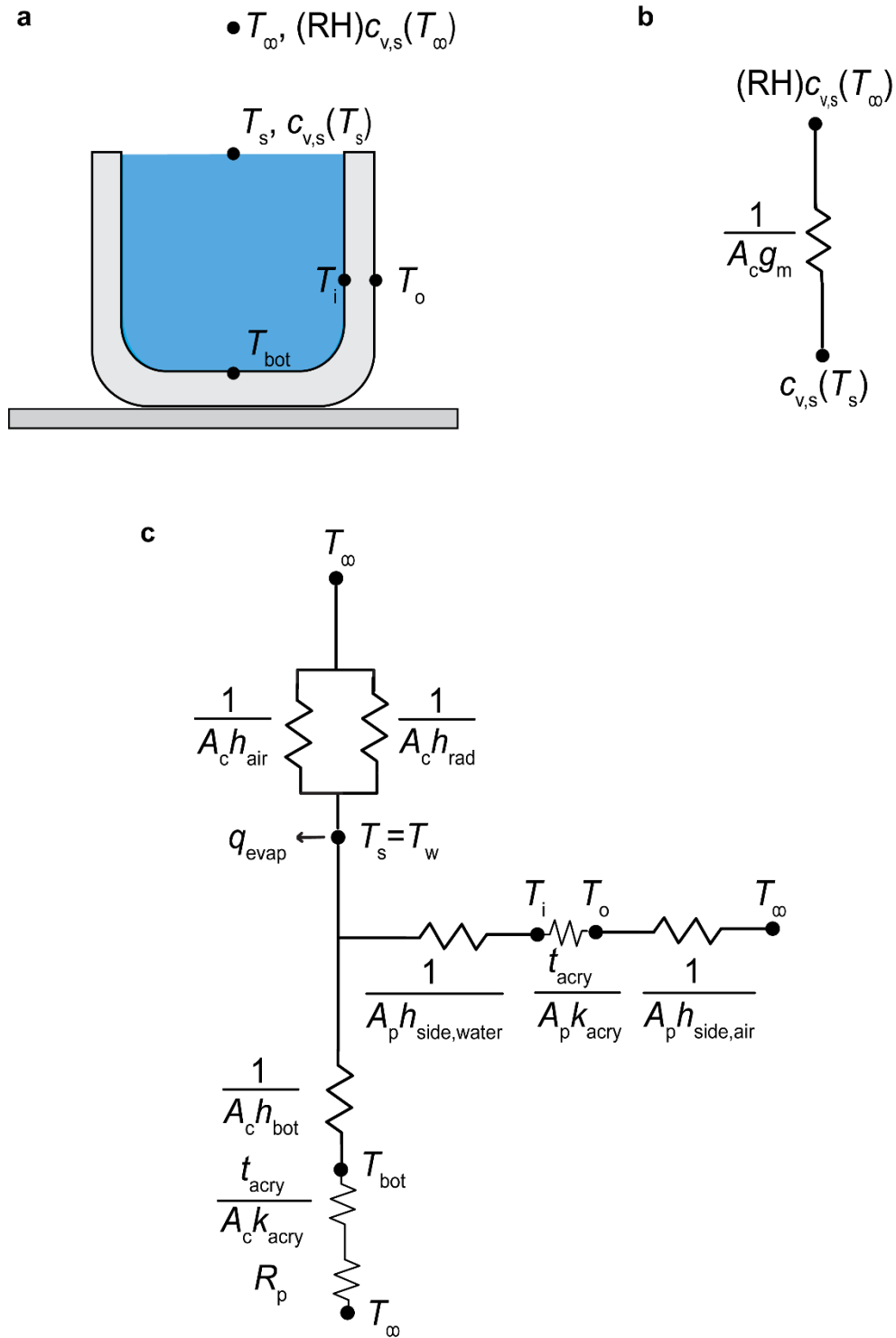


Fig. S2 Heat and mass transfer resistance network. (a) Heat and mass transfer schematic for water-only natural evaporation with temperature and vapor concentration nodes. (b) Mass transfer resistance network and (c) heat transfer resistance network used to calculate water-only evaporation rates from Supplementary Note S.2.

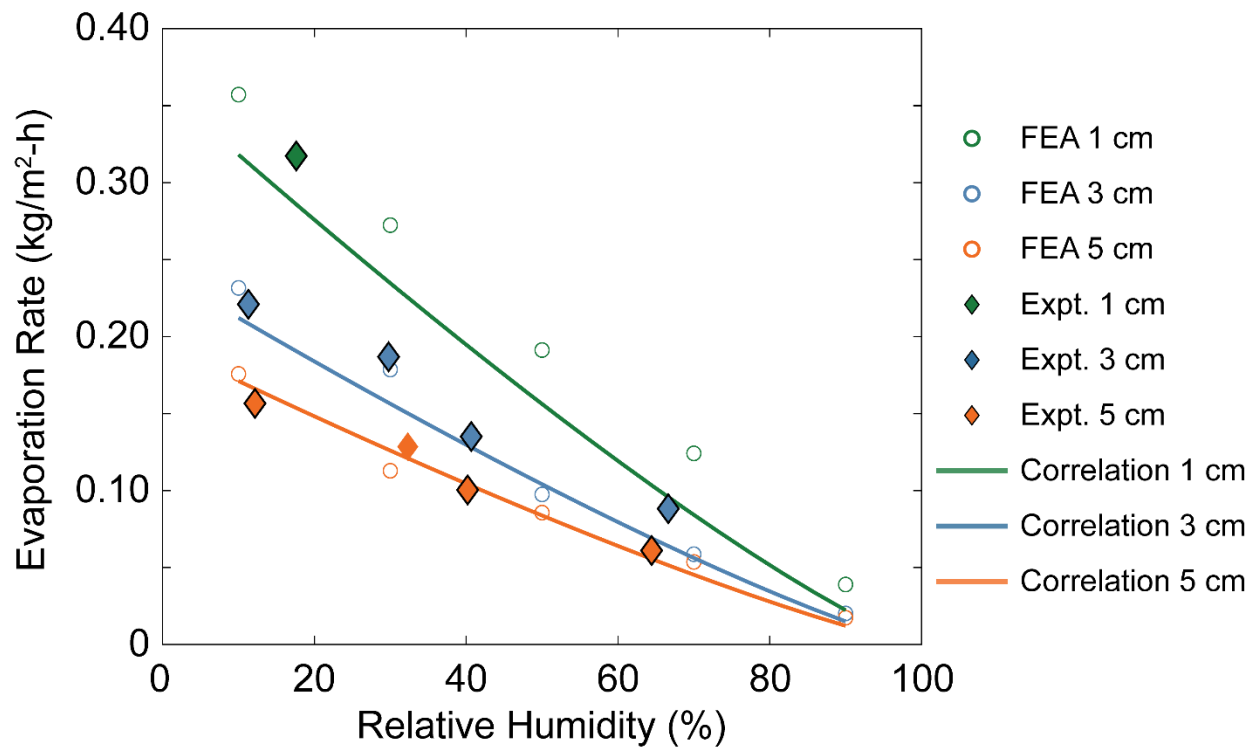


Fig. S3 Validation of correlation-based model. Predicted evaporation rate for different sized container diameters using the correlation model described in Supplementary Note S.2 and Fig. S2. Comparisons with FEA simulations and experiments are shown as well.

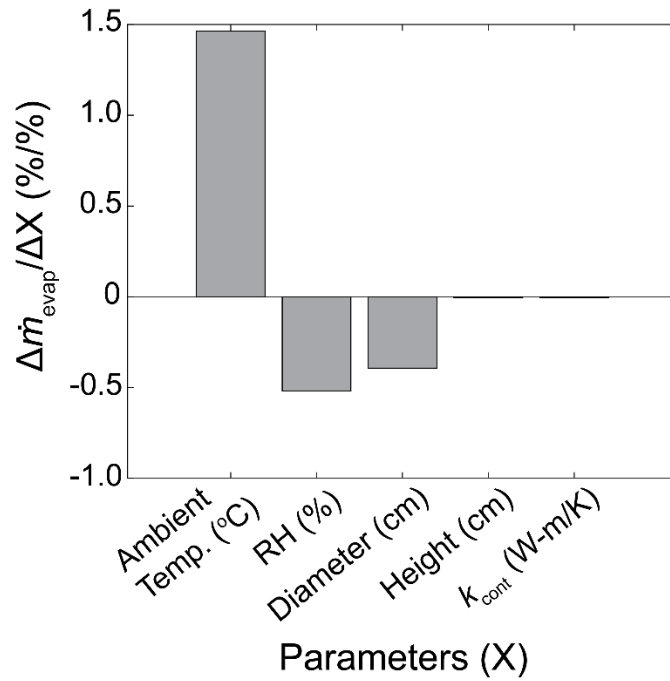


Fig. S4 Sensitivity analysis of the correlation model. The sensitivity of evaporation is calculated numerically by changing the base case parameters by 0.5% in both the positive and negative directions and calculating the relative change in evaporation rate predicted. The base case considered is a water-only interface evaporating into an ambient at 23 °C, an ambient RH of 30%, an evaporating diameter of 3 cm, a container wall thickness of 2 mm, a container height of 4 cm, and a thermal conductivity of the container at 0.19 W/m-K.

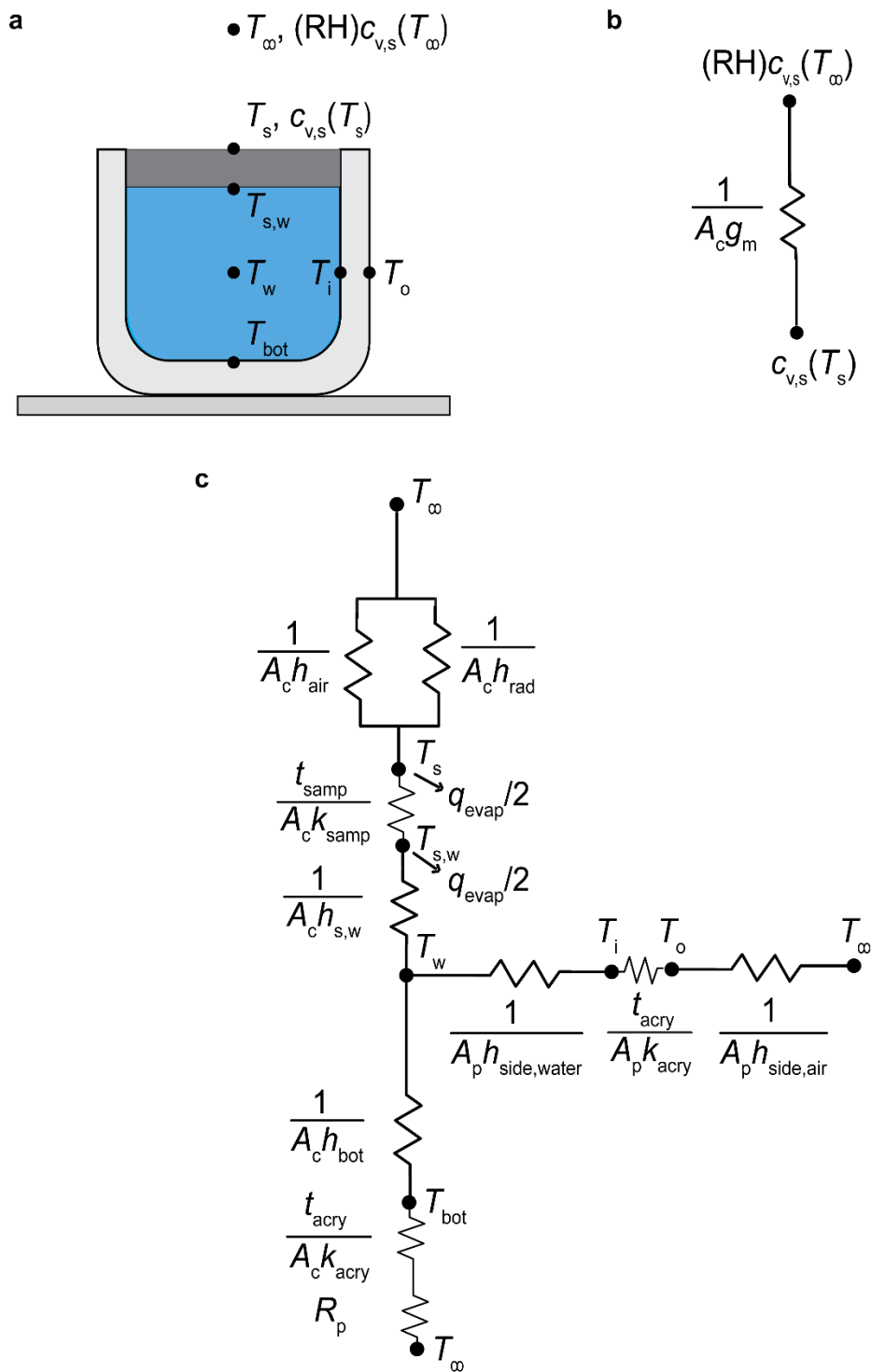


Fig. S5 Heat and mass transfer resistance network when there is latent heat reduction. (a) Heat and mass transfer schematic for porous sample natural evaporation with temperature and vapor concentration nodes. (B) Mass transfer resistance network and (C) heat transfer resistance network used to calculate evaporation rates for porous evaporators described in Supplementary Notes S.3-S.6.

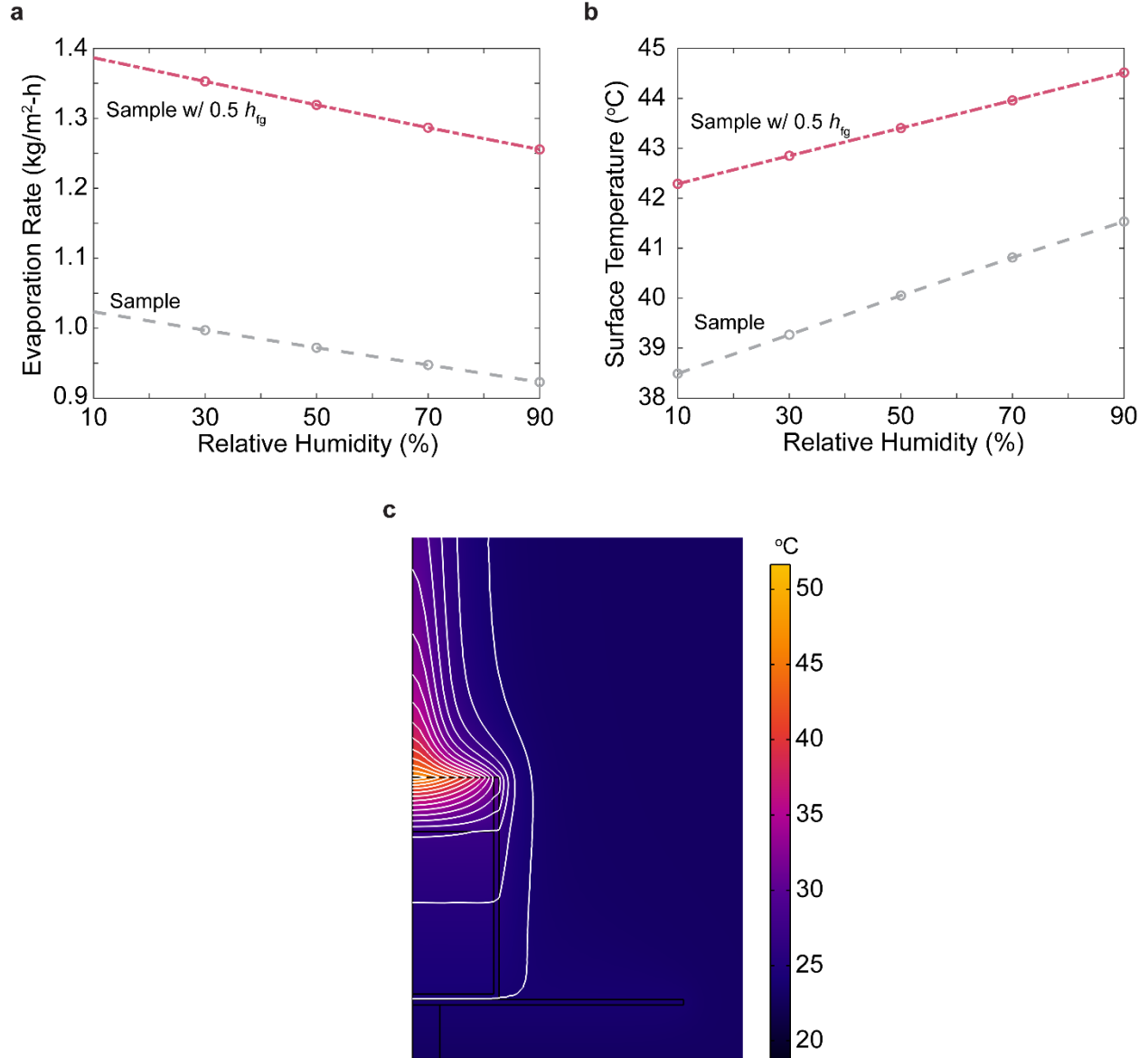


Fig. S6 FEA heat and mass transfer under solar irradiation. Simulated (a) evaporation rates and (b) average surface temperatures of porous sample during solar evaporation experiments. The evaporating diameter is set to 3 cm, the ambient temperature is set to 23 °C, and the sample thermal resistance in the height direction is 0.1 m²K/W. (c) Snapshot of steady-state temperature distribution after 2 hours of solar evaporation for a sample with no intermediate water states. The white lines represent isotherm contours.

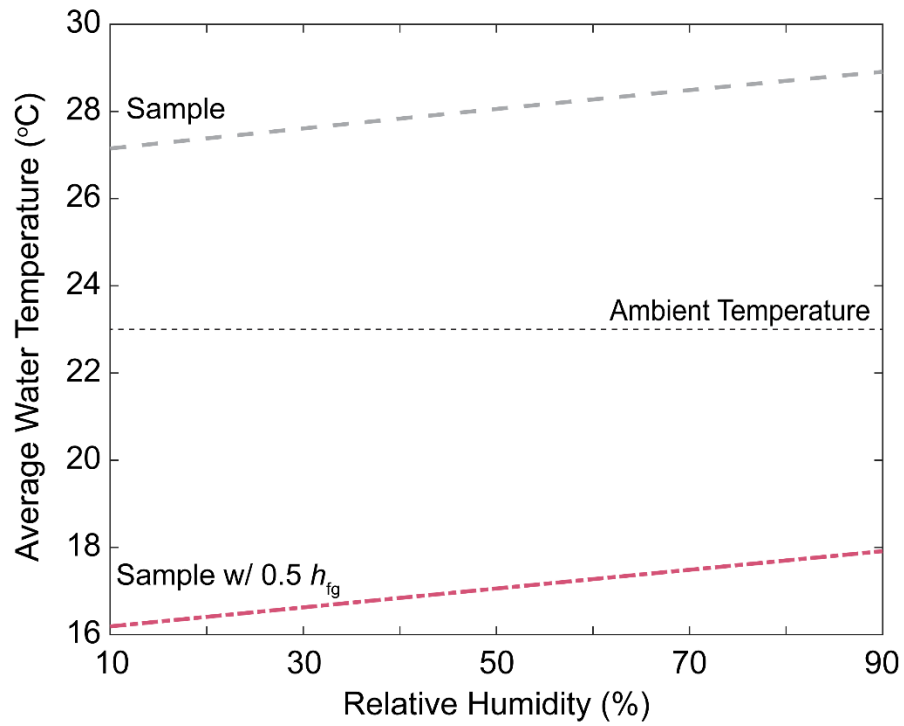


Fig. S7 Predicted average water temperature inside of the container under solar irradiation. The container size is set to 3 cm, sample resistance of 0.1 m²K/W, and ambient temperature of 23 °C in the correlation model. If latent heat is reduced by half, the water temperature is lower than ambient due to cooling effect at the sample-water interface.

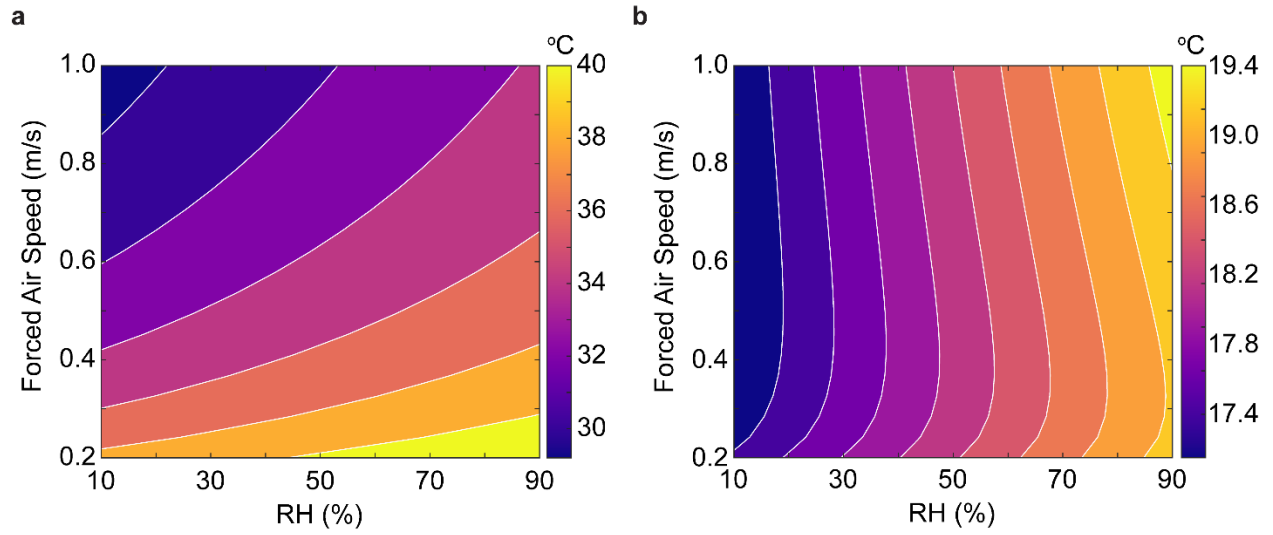


Fig. S8 Effect of forced convection. Predicted (a) surface temperature and (b) average water temperature of from evaporation of porous evaporators with reduced latent heat (half of bulk value) during solar evaporation under forced convection conditions in correlation model. Water temperature is again below the ambient temperature at 23 °C.

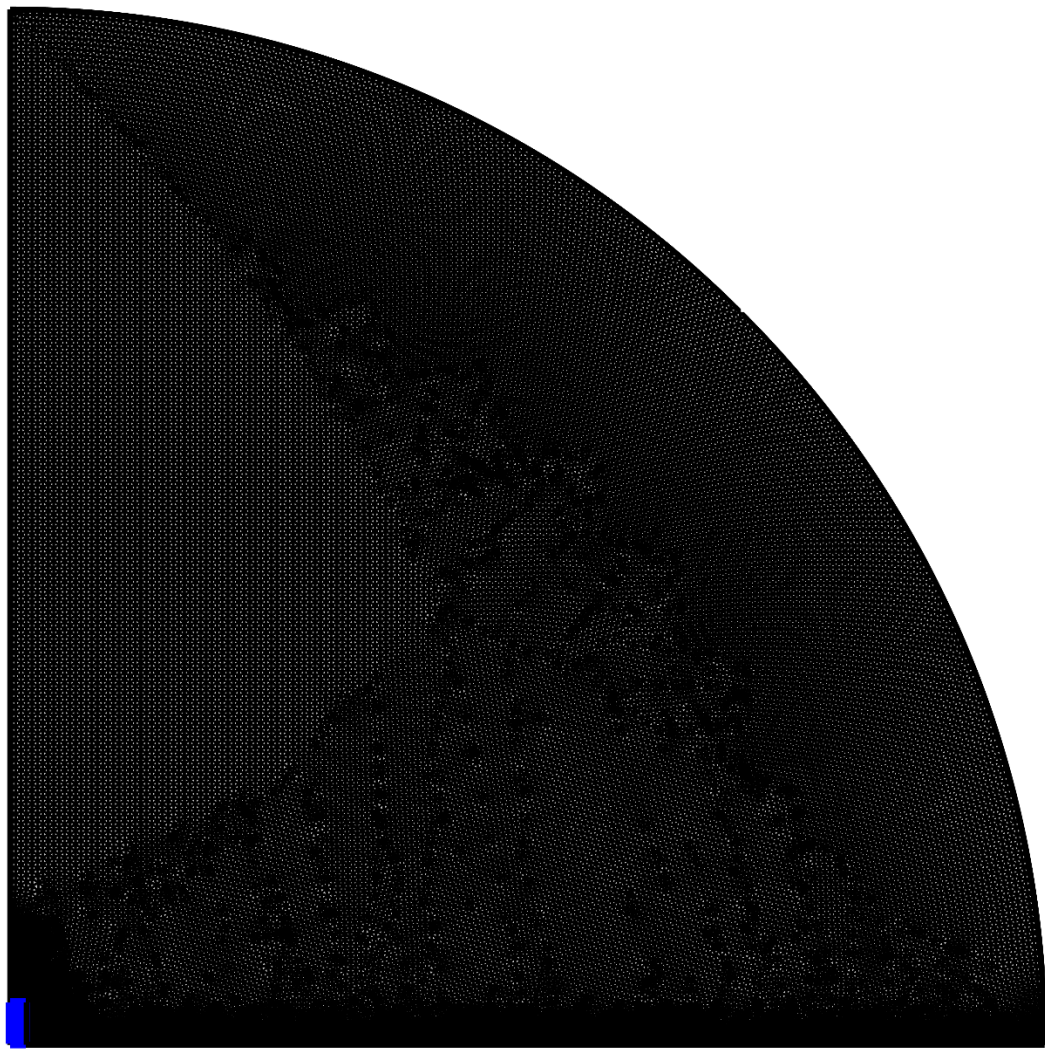


Fig. S9 Simulation domain. Full simulation domain with 1 meter radius for natural evaporation of pure water interfaces. The mesh representing the water container and liquid water inside is highlighted in blue for clarity.

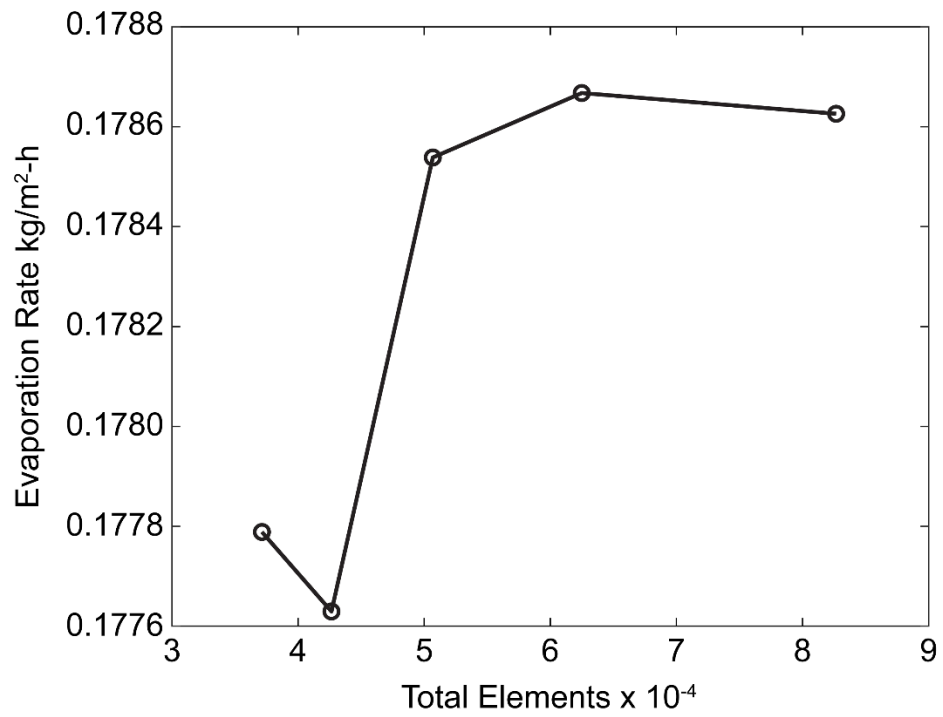


Fig. S10 Mesh sensitivity analysis on predicted evaporation rate for container with 1.5 cm radius evaporating into an ambient environment at 23 °C and 30% RH. The number of elements used for this condition reported in the main figure is 60264.

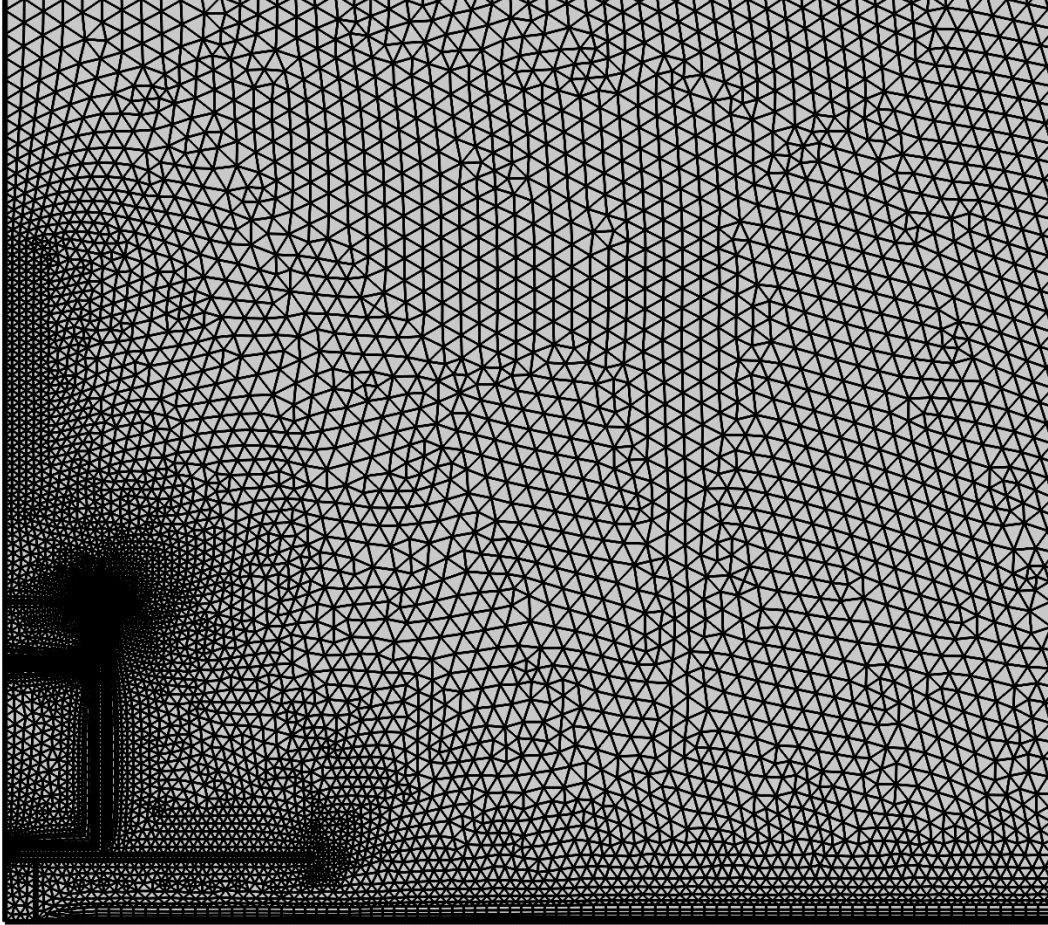


Fig. S11 Mesh used for solar interfacial-evaporation simulation. Zoomed in mesh for solar evaporation of samples in FEA simulations on top of an aluminum scale pan. Higher resolution mesh is used in the boundary layer regions on the evaporating surface and near solid/fluid interfaces. The hemispherical air domain size is reduced to 0.6 m to reduce computation time.

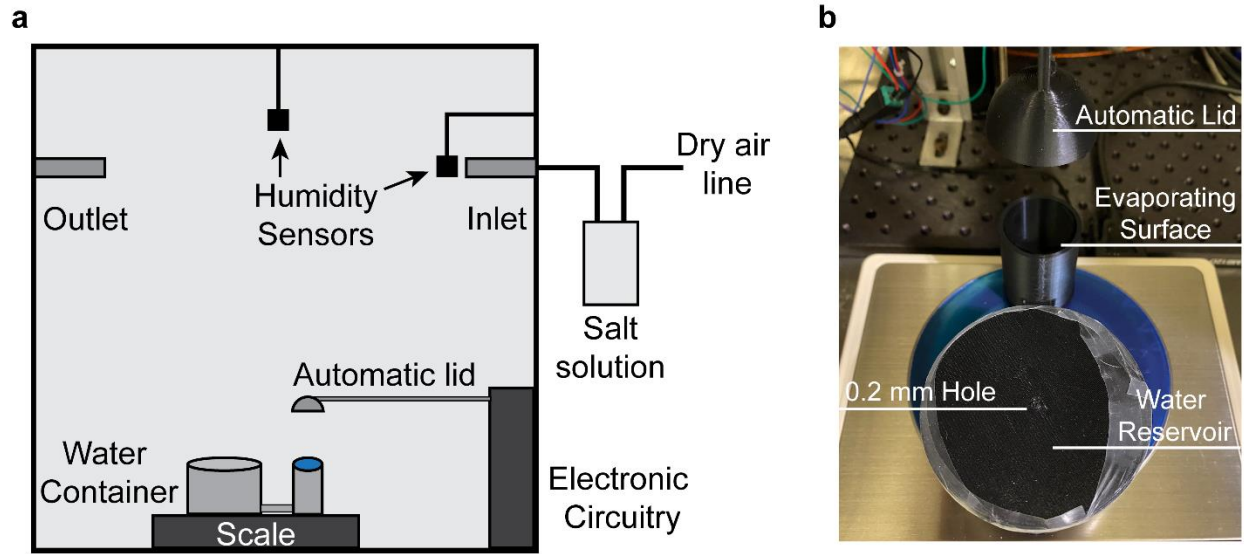


Fig. S12 Experimental set up. (a) Schematic of controlled humidity chamber setup with a dimension of 0.6 m in each direction. (b) Top view of the 3D printed polylactic acid container with water on the scale and the automatic lid lifted above the surface.

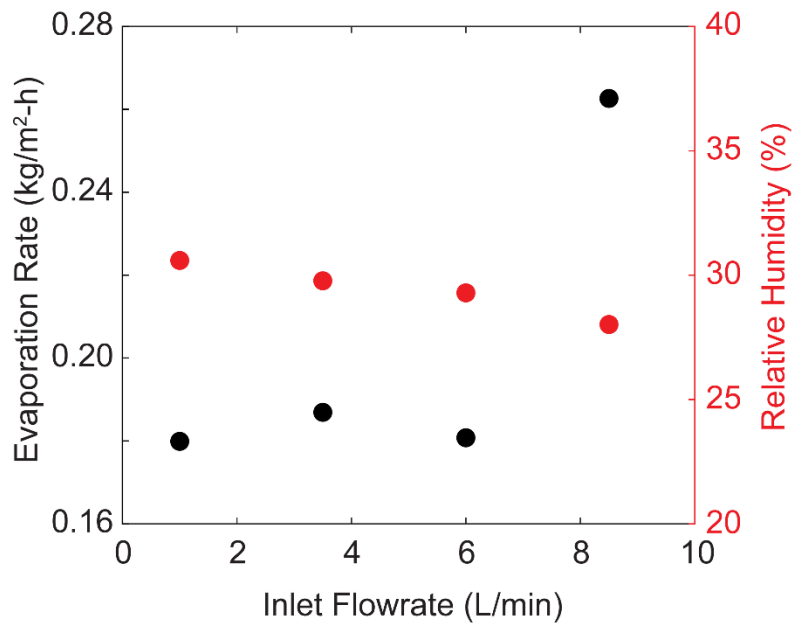


Fig. S13 Effect of inlet airflow. Dependence on evaporation rate with inlet airflow for water-only natural evaporation experiments. The experiments were conducted with a mean temperature of 24.62 °C. The difference in mean temperatures for each experiment was below 0.12 °C.

Table S1. Comparison of literature natural evaporation compared to model. Data shows the experimental testing conditions as well as the sample geometry. These values are used as inputs into the correlation model to predict water-only evaporation rate as described in Supplementary Note S.3.

Source	Size (cm)	Shape	RH (%)	Temp (°C)	Water Evap. Rate (kg/m ² -h)	Sample Evap. Rate (kg/m ² -h)	Predicted Water Evap. Rate (kg/m ² -h)
Study 1 ⁹	1	Square	45	25	0.011	0.019	0.201
Study 2 ¹⁰	1	Square	45	25	0.014	0.039	0.201
Study 3 ¹¹	1.6	Circle	45	25	0.073	0.099	0.169
Study 4 ¹²	3.2	Circle	31	20	0.081	0.141	0.124
Study 5 ¹³	3.5	Square	30	20	0.042	0.085	0.122
Study 6 ¹⁴	4.1	Circle	18.6	19.55	0.084	0.113	0.133
Study 7 ¹⁵	4.87	Circle	52.5	23	0.05	0.108	0.080
Study 8 ¹⁶	5	Circle	27	26	0.059	0.272	0.157
Study 9 ¹⁷	5.5	Square	45	25	0.024	0.059	0.106

Table S2. Comparison of this work's experimental data with correlation model.

Size (cm)	Shape	RH (%)	Temp (°C)	Measured Water Evap. Rate (kg/m ² -h)	Predicted Water Evap. Rate (kg/m ² -h)	Rel. Error to Model
1	Circle	17.60	24.07	0.3173	0.3072	3%
3	Circle	11.30	24.83	0.2210	0.2332	-5%
3	Circle	29.77	24.57	0.1869	0.1729	8%
3	Circle	40.67	24.66	0.1348	0.1425	-5%
3	Circle	66.63	24.74	0.0882	0.0711	24%
5	Circle	12.17	23.82	0.1566	0.1743	-10%
5	Circle	32.30	24.83	0.1285	0.1345	-4%
5	Circle	40.19	24.23	0.1004	0.1118	-10%
5	Circle	64.44	23.97	0.0610	0.0588	4%

REFERENCES

- 1 S. Chandrasekhar, *Hydrodynamic and Hydromagnetic Stability*, Dover Publications, New York, 1981.
- 2 V. Kadambi and R. M. Drake, *Free convection heat transfer from horizontal surfaces for prescribed variations in surface temperature and mass flow through the surface.*, Tech. Rept. Mech. Eng. HT-1, Princeton, 1960.
- 3 J. H. Lienhard IV and J. H. Lienhard V, *A Heat Transfer Textbook*, Phlogiston Press, Cambridge, 5th edn., 2020.
- 4 G. D. Raithby and K. G. T. Hollands, *Handbook of Heat Transfer*, McGraw-Hill, New York, 3rd edn., 1998.
- 5 J. R. Lloyd and W. R. Moran, *J. Heat Transfer*, 1974, **96**, 443–447.
- 6 S. W. Churchill and H. H. S. Chu, *Int. J. Heat Mass Transf.*, 1975, **18**, 1323–1329.
- 7 Adrian Bejan, *Convection Heat Transfer*, John Wiley & Sons, Inc., 4th edn., 2013.
- 8 S. W. Churchill and M. Bernstein, *J. Heat Transfer*, 1977, **99**, 300–306.
- 9 F. Zhao, X. Zhou, Y. Shi, X. Qian, M. Alexander, X. Zhao, S. Mendez, R. Yang, L. Qu and G. Yu, *Nat. Nanotechnol.*, 2018, **13**, 489–495.
- 10 X. Zhou, Y. Guo, F. Zhao, W. Shi and G. Yu, *Adv. Mat.*, 2020, **32**, 2007012.
- 11 W. Li, X. Li, W. Chang, J. Wu, P. Liu, J. Wang, X. Yao and Z. Z. Yu, *Nano Res.*, 2020, **13**, 3048–3056.
- 12 H. Zou, X. Meng, X. Zhao and J. Qiu, *Adv. Mat.*, 2023, **35**, 2207262.
- 13 Z. Yu, R. Gu, Y. Tian, P. Xie, B. Jin and S. Cheng, *Adv. Funct. Mater.*, 2022, **32**, 2108586.
- 14 A. Caratenuto and Y. Zheng, *Sci. Adv.*, 2024, **10**, 6368.
- 15 S. Lei, D. Huang, S. Liu, M. Chen, R. Ma, M. Zeng, D. Li, W. Ma, L. Wang and Z. Cheng, *J. Mater. Chem. A*, 2021, **9**, 15346–15354.
- 16 J. Chen, B. Li, G. Hu, R. Aleisa, S. Lei, F. Yang, D. Liu, F. Lyu, M. Wang, X. Ge, F. Qian, Q. Zhang and Y. Yin, *Nano Lett.*, 2020, **20**, 6051–6058.
- 17 Q. F. Guan, Z. M. Han, Z. C. Ling, H. Bin Yang and S. H. Yu, *Nano Lett.*, 2020, **20**, 5699–5704.